

# Highly Selective Methanol Synthesis Using Electrochemical CO<sub>2</sub> Reduction with Defect-Engineered Cu<sub>58</sub> Nanoclusters

Sourav Biswas, Tomoya Tanaka, Haohong Song, Masaki Ogami, Yamato Shingyouchi, Sakiat Hossian, Maho Kamiyama, Taiga Kosaka, Riki Nakatani, Yoshiki Niihori, Saikat Das, Tokuhisa Kawawaki,\* De-en Jiang,\* and Yuichi Negishi\*

Atomically precise copper nanoclusters (Cu NCs) exhibit significant potential as catalysts for the electrocatalytic reduction of CO<sub>2</sub>. However, the range of products achievable with these NCs has been somewhat constrained. This study presents an innovative design strategy to enhance the catalytic activity of Cu NCs by engineering their active sites. These active sites are formed here by introducing defects on cubic Cu NCs through the partial dislocation of Cu atoms at their vertices, which creates surface ligand vacancies. This dislocation further refines the internal cationic geometry by altering cuprophilic interactions, leading to distinct modifications in the edges and vertices of the cubic geometry. These unique Cu(I) atom arrangements within the cluster effectively influence product specificity during electrochemical CO<sub>2</sub> reduction. Density functional theory calculations correlate the enhanced selectivity for CH<sub>3</sub>OH in [Cu<sub>58</sub>H<sub>20</sub>(SPr)<sub>36</sub>(PPh<sub>3</sub>)<sub>7</sub>]<sup>2+</sup> (Pr = CH<sub>2</sub>CH<sub>2</sub>CH<sub>3</sub>) NC to the increased reactivity of edge Cu atoms in binding CO and CHO intermediates, compared to [Cu<sub>58</sub>H<sub>20</sub>(SPr)<sub>36</sub>(PPh<sub>3</sub>)<sub>8</sub>]<sup>2+</sup> and [Cu<sub>58</sub>H<sub>20</sub>(SEt)<sub>36</sub>(PPh<sub>3</sub>)<sub>6</sub>]<sup>2+</sup> (Et = CH<sub>2</sub>CH<sub>3</sub>) NCs. Thus, this work underscores the potential of tailored structural designs of atomically precise nanocatalysts in directing electrochemical CO<sub>2</sub> reduction toward unconventional products.

This situation emphasizes the urgent need for innovative solutions for environmental degradation and energy sustainability.<sup>[2]</sup> Amidst this challenge, a promising avenue emerges: harnessing the excess CO<sub>2</sub> in our environment as an energy source.<sup>[3]</sup> Among the diverse array of CO<sub>2</sub>-reduction methodologies, the catalyst-induced electrochemical reduction method has garnered significant attention.<sup>[4]</sup> Once the reduction approach is established, the efficacy of the catalysts has become a paramount global research concern. Consequently, a burgeoning research endeavor is underway worldwide to engineer an optimal catalyst for this electrochemical reduction process.<sup>[5]</sup> In the course of this journey, transition metal electrocatalysts have demonstrated their superiority over other contenders.<sup>[6]</sup> However, unraveling the complexities of catalyst performance proves to be a formidable challenge, considering the influential role played by factors such as material structure

## 1. Introduction


The increasing emission of carbon dioxide (CO<sub>2</sub>) into the atmosphere is a major concern in the face of global warming and climate change.<sup>[1]</sup> Despite efforts, the primary source—fossil fuel combustion to meet energy demands—continues unabated.

and size.<sup>[7]</sup> In response to this challenge, researchers are increasingly directing their attention toward achieving uniformity and smaller sizes, with nanoclusters (NCs) emerging as a promising avenue.<sup>[8]</sup>

Remarkably, gold and silver NCs have demonstrated notable success in efficiently reducing CO<sub>2</sub> to CO, a valuable feedstock

S. Biswas, S. Hossian, Y. Niihori, S. Das, Y. Negishi  
Research Institute for Science & Technology  
Tokyo University of Science  
1-3 Kagurazaka, Shinjuku-ku, Tokyo 162-8601, Japan  
E-mail: yuichi.negishi.a8@tohoku.ac.jp

T. Tanaka, M. Ogami, Y. Shingyouchi, M. Kamiyama, T. Kosaka,  
R. Nakatani  
Department of Applied Chemistry  
Tokyo University of Science  
1-3 Kagurazaka, Shinjuku-ku, Tokyo 162-8601, Japan

 The ORCID identification number(s) for the author(s) of this article can be found under <https://doi.org/10.1002/smssc.202400465>.

© 2024 The Author(s). Small Science published by Wiley-VCH GmbH. This is an open access article under the terms of the Creative Commons Attribution License, which permits use, distribution and reproduction in any medium, provided the original work is properly cited.

DOI: 10.1002/smssc.202400465

H. Song  
Interdisciplinary Materials Science  
Vanderbilt University  
Nashville, TN 37235, USA

T. Kawawaki  
Carbon Value Research Center  
Tokyo University of Science  
2641 Yamazaki, Noda, Chiba 278-8510, Japan  
E-mail: kawawaki@rs.tus.ac.jp

D. Jiang  
Department of Chemical and Biomolecular Engineering  
Vanderbilt University  
Nashville, TN 37235, USA  
E-mail: de-en.jiang@vanderbilt.edu

Y. Negishi  
Institute of Multidisciplinary Research for Advanced Materials  
Tohoku University  
Katahira 2-1-1, Aoba-ku, Sendai 980-8577, Japan

for the subsequent generation of fuel.<sup>[9]</sup> However, the focus has shifted to the formation of other NCs for achieving products with even higher energy densities. Among the higher energy density products, methanol (CH<sub>3</sub>OH) emerges as a standout option, boasting exceptional characteristics such as high energy density, ease of storage, and transportability, making it highly desirable as a fuel source.<sup>[10]</sup> Furthermore, the versatility of CH<sub>3</sub>OH extends beyond its role as a fuel. It serves as a raw material across a spectrum of industries including plastics, paints, silicone, and other chemical sectors, underscoring its pivotal importance. Despite its utility, the conventional steam methane reforming and dry reforming method of producing CH<sub>3</sub>OH emits substantial greenhouse gases under ultra-high pressure and high-temperature conditions, limiting its applicability in sustainable practices. Therefore, there is a growing interest in leveraging the electrochemical reduction of CO<sub>2</sub> to selectively produce CH<sub>3</sub>OH under normal temperature and pressure, offering a near-zero-emission pathway toward achieving carbon neutrality.<sup>[11]</sup>

Recent research has shed light on the remarkable potential of copper (Cu) NCs in electrochemical CO<sub>2</sub> reduction.<sup>[12]</sup> Unlike traditional NC-based catalysts, these Cu NCs possess a unique capability to yield predominant products such as formic acid (HCOOH), carbon monoxide (CO), and hydrocarbons during CO<sub>2</sub> reduction.<sup>[13]</sup> This breakthrough not only expands the repertoire of potential products but also signifies a substantial advancement in the pursuit of efficient CO<sub>2</sub> reduction methodologies. While Cu nanoparticles have been utilized in this domain for their versatility in product generation, the utility of Cu NCs remains somewhat limited within certain parameters.<sup>[14]</sup> Hence, there exists a compelling need to explore the potential of Cu NCs for producing a wider array of valuable products. It has been observed that various factors such as the NC architecture, number of constituent atoms, and ligands play pivotal roles in determining the catalytic activity of Cu NCs.<sup>[12,15]</sup> Additionally, defect sites on Cu NCs also play a crucial role in various catalytic reactions, although there is no study yet available on how these defects can tune the specificities of CO<sub>2</sub>-reduction products.<sup>[16]</sup> This presents an opportunity to fine-tune the inherent properties of Cu NCs to produce additional beneficial compounds beyond the regular products efficiently.

In the context outlined earlier, we employed defect-induced [Cu<sub>58</sub>H<sub>20</sub>(SPr)<sub>36</sub>(PPh<sub>3</sub>)<sub>7</sub>]<sup>2+</sup> (Pr = CH<sub>2</sub>CH<sub>2</sub>CH<sub>3</sub>) (Cu<sub>58</sub>-I) and [Cu<sub>58</sub>H<sub>20</sub>(SEt)<sub>36</sub>(PPh<sub>3</sub>)<sub>6</sub>]<sup>2+</sup> (Et = CH<sub>2</sub>CH<sub>3</sub>) (Cu<sub>58</sub>-II) NCs as catalysts for the highly selective electrochemical reduction of CO<sub>2</sub>. The remarkable selectivity of the reduction product and the catalytic activity primarily stem from the distinctive structural architecture of the catalyst. Comparative analysis with a regular [Cu<sub>58</sub>H<sub>20</sub>(SPr)<sub>36</sub>(PPh<sub>3</sub>)<sub>8</sub>]<sup>2+</sup> (Cu<sub>58</sub>) NC highlights the superiority of the surface ligand vacancy and the consequent rearrangement of Cu(I) atoms. These structural features greatly enhance the efficacy of the electrochemical reduction approach for CO<sub>2</sub>. However, the specificities have some limitations, which are finely adjusted by the structural architecture of the NC catalyst. Theoretical studies have identified the active catalytic sites, which are closely associated with the vacant ligand sites. The rearrangement in these sites predominantly dictates the selectivity of the product, emphasizing the crucial role played by the architecture of the NC in governing the catalytic process.

## 2. Results and Discussion

### 2.1. Synthesis and Structural Architecture

Herein, we synthesized Cu<sub>58</sub>-I and Cu<sub>58</sub>-II NCs by following our previously reported protocol for Cu<sub>58</sub> NC synthesis.<sup>[17]</sup> In the case of Cu<sub>58</sub>-I NC, the presence of one fewer PPh<sub>3</sub> unit compared to the regular Cu<sub>58</sub> NC is achieved by adjusting the composition of the ligands while maintaining the overall integrity of the NC architecture. However, when attempting to further decrease the number of PPh<sub>3</sub> units to six, as seen in Cu<sub>58</sub>-II NC, simply adjusting the ligand composition was insufficient. Instead, we achieved this by changing the thiolate ligand precursor from (SPr) to (SEt). The reduction in the carbon chain facilitated the stabilization of the NC despite the reduced number of PPh<sub>3</sub> units.

In a typical synthesis, a Cu(I) precursor was subjected to treatment with PPh<sub>3</sub> and specific thiol ligand in a solvent mixture containing acetonitrile and chloroform. The reaction proceeded until the addition of excess NaBH<sub>4</sub>. Upon completion, the resulting precipitate formed deep red-colored block crystals through the slow evaporation of the solvent at room temperature. The single-crystal X-ray diffraction (SCXRD) revealed Cu<sub>58</sub>-I NC crystallizes in a trigonal crystal system with a P-3 (No. 147) space group (Table S1, Supporting Information). While Cu<sub>58</sub>-II NC crystallizes in a triclinic crystal system with a P-1 (No. 2) space group (Table S2, Supporting Information).

Although the obtained crystalline structures do not share a common crystal system, we observed a quite similar cubic arrangement of Cu(I) atoms which is surrounded by protective ligands in both Cu<sub>58</sub>-I and Cu<sub>58</sub>-II NCs, similar to what was observed in the regular Cu<sub>58</sub> NC (Figure 1). Our detailed examination revealed that both Cu<sub>58</sub>-I and Cu<sub>58</sub>-II exhibit nested Keplerian architectures, featuring Cu<sub>8</sub> cubic cores (Figure S1, Supporting Information) encircled by four concentric Cu(I) shells (Figure S2, Supporting Information). In both cases, the innermost Cu<sub>6</sub> octahedron shell is positioned at the center, linking the Cu(I) atoms from each face of the Cu<sub>8</sub> cubic core. The Cu<sub>24</sub> rhombicuboctahedron shell shapes the facets of the overall cubic architecture by creating a middle plane with four Cu(I) atoms. Additionally, the Cu<sub>12</sub> cuboctahedron shell contributes to the edge centers of the overall cubic architecture, while the outermost Cu<sub>8</sub> cubic shell forms the vertices of the cube. These observations align with our previous findings on Cu<sub>58</sub> NC.<sup>[17]</sup> Furthermore, we detected three types of ligands (thiolate, PPh<sub>3</sub> and hydride) arranged in specific geometries to protect these NCs by forming ligand shells. The hydride ligands are positioned interstitially in both cases, connecting the core and the inner shell by forming H<sub>8</sub> cubic and an H<sub>12</sub> icosahedron ligand shell geometries (Figure S3, Supporting Information). Despite the change in the carbon chain length, the thiolate ligands in both NCs are arranged similarly into two distinct geometries: an S<sub>12</sub> icosahedron and an S<sub>24</sub> truncated cubic ligand shell (Figure S4, Supporting Information). These thiolate ligand shells serve to protect the edges and facets of the cube, ensuring structural stability and integrity. However, a significant change is first visible in the attachment of the PPh<sub>3</sub> ligands. In the regular Cu<sub>58</sub> NC, eight PPh<sub>3</sub> ligands form a complete cubic ligand shell (P<sub>8</sub>) around the NC, which is not observed in Cu<sub>58</sub>-I and Cu<sub>58</sub>-II NCs

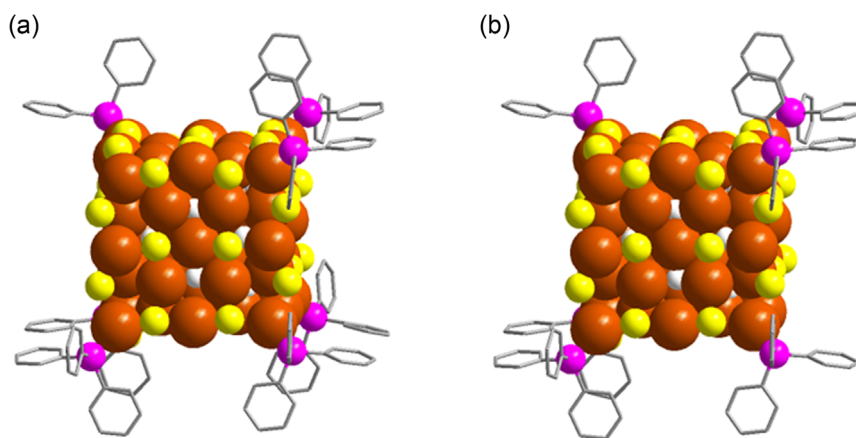


**Figure 1.** The overall structural architecture of a)  $\text{Cu}_{58}\text{-I}$  and b)  $\text{Cu}_{58}\text{-II}$  NCs. All the carbon parts are removed from the thiolate ligands, anionic part, and the solvent part also removed for the clarity. Hydrogen atoms are removed from the phenyl rings. Color legend: Cu, brown; S, yellow; P, violet; H, white; and C, grey stick.

(Figure 2a–c). In  $\text{Cu}_{58}\text{-I}$  NC, we observed one vacant site in the  $\text{P}_8$  ligand shell, where one vertex Cu atom of the  $\text{Cu}_8$  cubic shell is exposed due to this vacancy. In contrast,  $\text{Cu}_{58}\text{-II}$  NC exhibited two vacant sites diagonally in the  $\text{P}_8$  ligand shell, exposing two Cu atoms from the  $\text{Cu}_8$  cubic shell. Since the construction of the  $\text{P}_8$  ligand shell relies on direct Cu–P bond formation involving the Cu(I) atoms from the  $\text{Cu}_8$  cubic shell, we anticipate irregularities in that cationic shell, which may prevent the  $\text{PPh}_3$  ligands from attaching at those specific positions. As we have already discussed the formation of the cationic shells is followed similarly however, we observed a notable geometric distortion in

the outermost  $\text{Cu}_8$  cubic shells compared to  $\text{Cu}_{58}$  NC (Figure 2d, e and Figure S5, Supporting Information). We identified that this outer  $\text{Cu}_8$  cubic shell was formed via thiolate bridging, lacking direct connections to the Cu(I) atoms of the inner shells.<sup>[17]</sup> As a result, we noticed a distinct directional arrangement of the Cu–S<sub>3</sub> moiety bridging, forming each vertex of the cube. However, here the distortions arise from the partial dislocation of vertex Cu(I) atoms, disrupting their typical outward directional bonding with the bridging thiolate ligands (Figure 2e,f). Due to this inward distortion of the Cu(I) atom alters the distance between Cu(I) atoms and those forming the adjacent facets contributing from

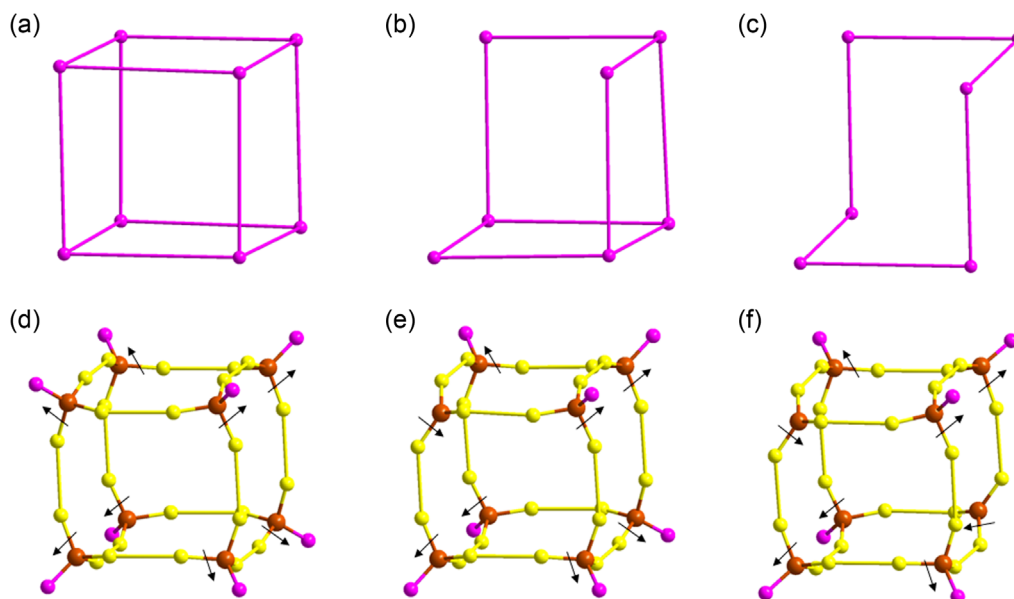


**Figure 2.** a) Complete cubic  $\text{P}_8$  shell of  $\text{Cu}_{58}$  NC, b) incomplete cubic  $\text{P}_7$  shell of  $\text{Cu}_{58}\text{-I}$  NC, c) incomplete cubic  $\text{P}_6$  shell of  $\text{Cu}_{58}\text{-II}$  NC, d) outward and inward directional arrangement of  $\text{Cu}_8$  cubic shell associated with the attached ligands in  $\text{Cu}_{58}$  NC, e) outward and inward directional arrangement of  $\text{Cu}_8$  cubic shell associated with the attached ligands in  $\text{Cu}_{58}\text{-I}$  NC and f) outward and inward directional arrangement of  $\text{Cu}_8$  cubic shell associated with the attached ligands in  $\text{Cu}_{58}\text{-II}$  NC. Bonds between the P–P and S–S are virtual. All the carbon parts are removed from the thiolate and  $\text{PPh}_3$  ligands. Color legend: Cu, brown; S, yellow; P, violet.

the Cu<sub>24</sub> rhombicuboctahedron shell. In Cu<sub>58</sub>-I NC the average distance decreases to 2.665 Å from 3.4108 ± 0.0146 Å (average from the other corners). Similarly, in Cu<sub>58</sub>-II NC, the average distance decreases to 2.6713 ± 0.0065 Å from 3.4032 ± 0.0173 Å (average from the other corners), indicating strong cuprophilic interactions at the defect sites (Figure S6, Supporting Information). These additional interactions help alleviate the strain from the distortion of the Cu(I) atom at the dislocation sites and stabilize the overall cluster structures. However, this inward orientation of the Cu(I) atom at the vertex sites presents challenges for the attachment of PPh<sub>3</sub> ligands, likely due to steric crowding. This difficulty in ligand attachment constitutes the primary reason for the observed surface ligand vacancies. Therefore, this vacancy directly stems from the altered bonding environment induced by the distortion of the Cu(I) atoms in the outermost shell.

Further investigation reveals that at each defect vertex site, additional cuprophilic interactions with three adjacent Cu atoms from neighboring facets disrupt the regular geometries of the adjacent shells. More specifically the rhombicuboctahedron shell is formed by connecting eight triangular Cu frames, each maintaining a fixed distance from the vertex Cu atoms of the Cu<sub>8</sub> cubic core. However, at the defect sites, we observed a change in the interaction between these triangular Cu frames. In the Cu<sub>58</sub>-I NC, this distance extends to 3.0016 Å, while the average distance at the other ends is 2.8766 ± 0.0319 Å. For the Cu<sub>58</sub>-II NC, this distance extends to 3.0253 ± 0.0099 Å, with the average distance at the other ends being 2.8876 ± 0.0464 Å (Figure S7, Supporting Information). Additionally, there is an observed alteration in the interatomic distances between these triangular Cu frames and the surrounding vertices of the Cu<sub>8</sub> cubic core (Figure S8, Supporting Information). We noted a reduction in the average distance at the defect sites compared to the regular sites for both NCs. The shorter interatomic distances indicate an associated inward displacement strain of the triangular Cu frames, generated by the dislocation of the Cu atom in the outermost cationic shell. Consequently, the rhombicuboctahedron shell of both NCs experiences distortions, spreading to the nearby edge centers contributed by the Cu<sub>12</sub> cuboctahedron shell. We found that the distances between the edge-center Cu atoms on each constituent vertex can be categorized into two groups. For the defective sides, the distances between the three adjacent edge-centers are ≈ 6.2292 ± 0.0004 Å, while the distances between the edge-centers on the remaining vertices average 5.878 ± 0.0377 Å for Cu<sub>58</sub>-I NC. For Cu<sub>58</sub>-II NC, the distances are 6.2411 ± 0.0227 Å and 5.8269 ± 0.0434 Å, respectively (Figure S9, Supporting Information). These observations clearly demonstrate the impact of the distortion of the outer Cu(I) atoms on the inner shell geometry. On the other hand, this surface ligand vacancy directly exposes the defective vertex Cu atoms and indirectly exposes several neighboring facets and edges of these cubic NCs. Notably, the outward orientation of the edge-center Cu atoms relative to others presents intriguing possibilities, as these edge-center atoms, along with the vertex Cu atom at the defect sites, may potentially serve as catalytic sites (Figure S10, Supporting Information). However, the distances between these atoms vary because the vertex-to-vertex distances change during the formation of the defect-induced structural architecture,

which may uniquely affect their catalytic properties (Figure S11, Supporting Information).

## 2.2. Characterization of NCs and their Stability

In the positive mode electrospray ionization-mass spectrometry (ESI-MS), a discernible peak at  $m/z = 3204.74$  unequivocally affirms the existence of the molecular peak corresponding to [Cu<sub>58</sub>H<sub>20</sub>(SPr)<sub>36</sub>(PPh<sub>3</sub>)<sub>0</sub>]<sup>2+</sup> (Figure 3). However, achieving the molecular cluster peak featuring all the triphenylphosphine units attached to the cluster node poses considerable challenges due to its dynamic nature.<sup>[16a,18]</sup> Additionally, this task becomes even more difficult when defects are present in the structure. Nevertheless, we managed to attribute some of these units,  $m/z = 3335.78$ , 3467.83, and 3729.95 correspond to [Cu<sub>58</sub>H<sub>20</sub>(SPr)<sub>36</sub>(PPh<sub>3</sub>)<sub>1</sub>]<sup>2+</sup>, [Cu<sub>58</sub>H<sub>20</sub>(SPr)<sub>36</sub>(PPh<sub>3</sub>)<sub>2</sub>]<sup>2+</sup>, and [Cu<sub>58</sub>H<sub>20</sub>(SPr)<sub>36</sub>(PPh<sub>3</sub>)<sub>4</sub>]<sup>2+</sup>, respectively in Cu<sub>58</sub>-I NC. Conversely a different fragmentation pattern is observed in Cu<sub>58</sub>-II NC where the peaks  $m/z = 3083.34$ , 3214.27, 3346.32 and 3477.36 correspond to [Cu<sub>58</sub>H<sub>20</sub>(SEt)<sub>36</sub>(PPh<sub>3</sub>)<sub>1</sub>]<sup>2+</sup>, [Cu<sub>58</sub>H<sub>20</sub>(SEt)<sub>36</sub>(PPh<sub>3</sub>)<sub>2</sub>]<sup>2+</sup>, and [Cu<sub>58</sub>H<sub>20</sub>(SEt)<sub>36</sub>(PPh<sub>3</sub>)<sub>3</sub>]<sup>2+</sup> and [Cu<sub>58</sub>H<sub>20</sub>(SEt)<sub>36</sub>(PPh<sub>3</sub>)<sub>4</sub>]<sup>2+</sup>. So, the associated peaks in each cluster confirm the presence of the hydrides and their charge states, along with the different fragmentation patterns based on the defective structural architecture. The stability and dispersibility of the Cu<sub>58</sub>-I and Cu<sub>58</sub>-II NC in solution medium are confirmed by transmission electron microscope (TEM) images, which show that their sizes are consistent with those measured by the SCXRD (Figure S12, Supporting Information). Given the highly stable nature of the synthesized NC in the solution medium, we proceeded to examine the effects of such defects on the optical properties. However, no changes were observed in the UV-vis absorbance spectrum in the solvent medium compared to our previously reported Cu<sub>58</sub> NC (Figure S13, Supporting Information). So, it can be assumed that the distortion in the vertex Cu(I) atoms and the associated ligand vacancies have no impact on their electronic charge transition.

## 2.3. Preparation of Catalysts and Associated Characterizations

As per our previous discussions, in our pursuit of the perfect catalyst for electrochemically reducing CO<sub>2</sub> into a valuable energy feedstock, we aim to utilize the Cu<sub>58</sub>-I and Cu<sub>58</sub>-II NCs and evaluate their efficacy against the regular Cu<sub>58</sub> NC. For the electrochemical evaluation, thin film electrodes were fabricated utilizing the spray coating technique. This involved spray-casting a slurry of the NC containing Carbon Black (CB) onto a thin carbon paper (CP) substrate as depicted in the experimental section. We confirmed that there was no change in the electronic and geometric structure of Cu<sub>58</sub>-I and Cu<sub>58</sub>-II NCs during the loading processes by the X-ray absorption fine structure (XAFS) spectra (Figure 4 and Figure S14, Supporting Information). The X-ray absorption near-edge structure (XANES) spectrum at the Cu K-edge for both the Cu<sub>58</sub>-I and Cu<sub>58</sub>-II NCs, as well as the loaded catalysts (Cu<sub>58</sub>-I NC/CB and Cu<sub>58</sub>-II NC/CB), demonstrates excellent alignment, indicating the electronic stability of these NCs after loading on CB. In both cases, the pre-edge peak ≈ 8980 resembles that of standard Cu<sub>2</sub>O, suggesting the presence of Cu(I) species in all cases



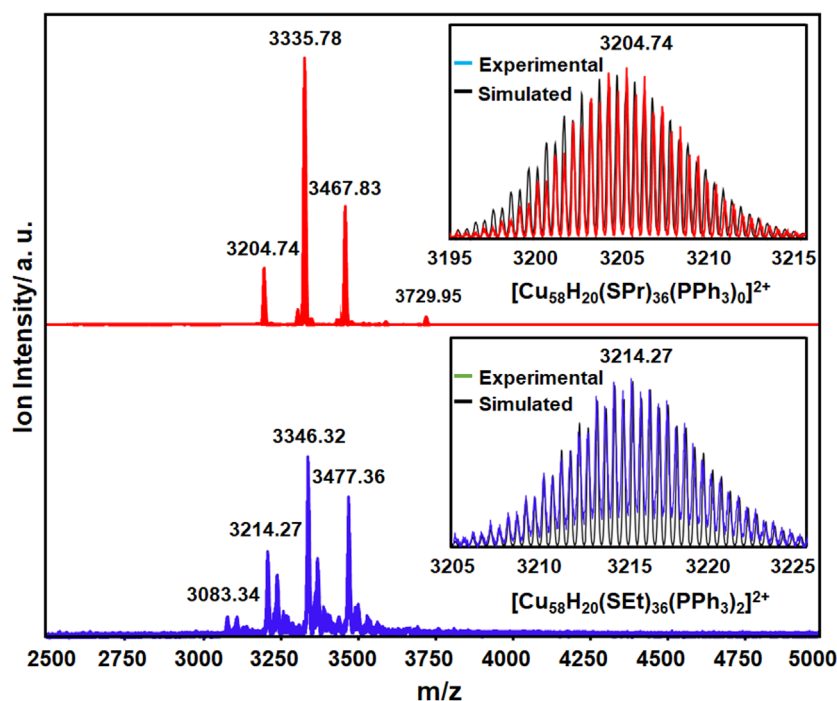


**Figure 3.** Positive mode ESI mass spectra of  $\text{Cu}_{58}$ -I and  $\text{Cu}_{58}$ -II NCs. Inset is showing the matching of experimental and simulated peak of  $[\text{Cu}_{58}\text{H}_{20}(\text{SPr})_{36}(\text{PPh}_3)_0]^{2+}$  and  $[\text{Cu}_{58}\text{H}_{20}(\text{SET})_{36}(\text{PPh}_3)_2]^{2+}$ .

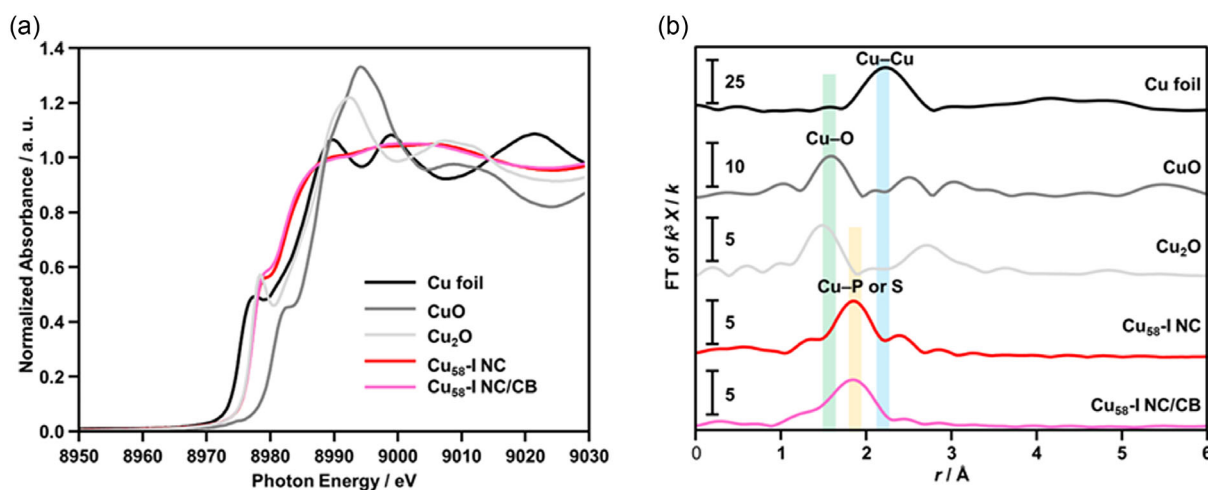


**Figure 4.** Cu K-edge a) XANES and b) FT-EXAFS spectra of  $\text{Cu}_{58}$ -I NC and  $\text{Cu}_{58}$ -I NC-loaded catalysts ( $\text{Cu}_{58}$ -I NC/CB). In (a,b) spectra of Cu foil, CuO powder and  $\text{Cu}_2\text{O}$  powder are also shown for comparison.

(Figure 4a and Figure S14a, Supporting Information). Fourier transforms-extended X-ray absorption fine structure (FT-EXAFS) spectra at the Cu K-edge reveal a distinct geometric arrangement in the  $\text{Cu}_{58}$ -I and  $\text{Cu}_{58}$ -II NCs, indicating a modified ligand environment compared to the standard sample, a characteristic maintained even after loading onto CB (Figure 4b and Figure S14b, Supporting Information). Notably, the peak at  $\approx 1.8$  Å in the FT-EXAFS is attributed to Cu–P or Cu–S bonding

in both NCs. Further analysis through R-space extended X-ray absorption fine structure (EXAFS) corroborates these observations, highlighting differences from the standard sample spectra while retaining their features upon loading (Figure S15, Supporting Information). Meanwhile, we also confirm the size of these NCs is retained upon loading on the CB surface through the TEM images (Figure S16, Supporting Information).

## 2.4. Electrochemical Performance

The electrochemical performance of all these NCs was thoroughly evaluated across a range of constant voltages (−0.6 to −0.9 V vs RHE) using CO<sub>2</sub>-saturated 0.1 M KHCO<sub>3</sub> aq. as an electrolyte in a gas-flow H-type cell setup. Subsequently, a comprehensive analysis employing gas chromatography (GC) and <sup>1</sup>H NMR was conducted to characterize the gas and liquid products, respectively. The linear sweep voltammetry (LSV) and cyclic voltammetry of these nanoclusters (NCs) under a CO<sub>2</sub> atmosphere (Figure S17, Supporting Information) showed that Cu<sub>58</sub>-II NC exhibited the highest reduction current at −0.9 V versus RHE, followed by Cu<sub>58</sub>-I NC and then Cu<sub>58</sub> NC. These initial results suggest that corner defect sites are likely responsible for initiating the reduction reaction. Our detailed findings revealed that, despite having similar overall geometrical architectures, these NCs yield different products during the electrocatalytic reduction reaction. We attribute this to variations in the distortion of their cationic shell geometry and surface ligand vacancies, which influence their reactivity by creating preferred catalytic sites. We observed at a potential range of −0.7 to −0.9 V (vs RHE) H<sub>2</sub>, CO and CH<sub>3</sub>OH are the primary products for Cu<sub>58</sub>-I NC (Figure 5a and Figure S18, Supporting Information) whereas H<sub>2</sub>, CO and HCOOH for Cu<sub>58</sub>-II NC (Figure 5b and Figure S19, Supporting Information). According to the Faradic Efficiency (FE) analysis, we observed that hydrogen evolution reaction (HER) is dominant (FE<sub>H<sub>2</sub></sub> > 50%) in the case of Cu<sub>58</sub>-II NC.

This dominance is attributed to the higher number of defect sites with more exposed edges and vertices, making the cluster surface easily accessible for the HER reaction. In contrast, Cu<sub>58</sub>-I NC, which features a single ligand vacancy with limited distortions and exposed sites, selectively produced CH<sub>3</sub>OH with a maximum FE<sub>CH<sub>3</sub>OH</sub> of ≈54% at −0.7 V (vs RHE). Comparing this with Cu<sub>58</sub> NC, which produces only CO as the CO<sub>2</sub>RR product due to its fewer reactive sites, highlights the significant impact of structural architecture on product selectivity and efficiency in CO<sub>2</sub>RR processes (Figure 5c and Figure S20, Supporting Information). The comparison of the associated current densities of the products for both Cu<sub>58</sub>-I and Cu<sub>58</sub>-II NCs further displayed their variable reactivities (Figure 5d,e). Especially, the currents of the products based on CO<sub>2</sub>RR were higher for Cu<sub>58</sub>-I NC (*j*<sub>CH<sub>3</sub>OH</sub> and *j*<sub>CO</sub>) than for Cu<sub>58</sub>-II NC (*j*<sub>HCOOH</sub> and *j*<sub>CO</sub>), due to the favorable electronic/geometric structure of Cu<sub>58</sub>-I NC for CO<sub>2</sub>RR. It becomes evident that the structural configuration of Cu<sub>58</sub>-I NC exhibits a favorable propensity for CH<sub>3</sub>OH selectivity, demonstrating variability across a broad potential range. Notably, as increasingly negative potentials were applied, the selectivity for CH<sub>3</sub>OH in CO<sub>2</sub>RR gradually decreased to ≈44% at −0.9 V, while the production of associated H<sub>2</sub> and CO increased. This trend became more pronounced at −1.0 V, where FE<sub>CO</sub> rose to ≈16% and the selectivity for CH<sub>3</sub>OH dropped to ≈37% (Figure S21, Supporting Information). According to the theoretical redox potentials, the formation of CO (−0.10 V vs RHE) and H<sub>2</sub> (0.00 V vs RHE) requires slightly higher overpotentials compared to methanol

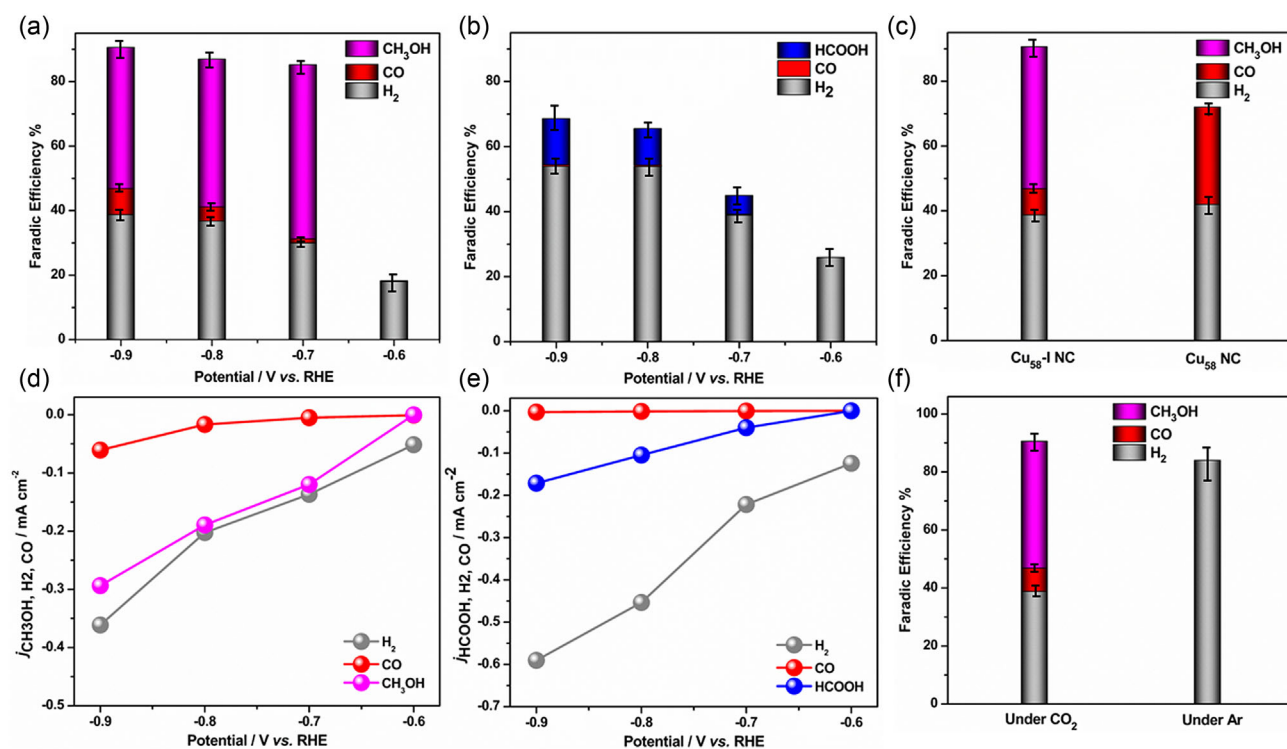


**Figure 5.** Electrocatalytic performances for CO<sub>2</sub>RR in 0.1 M KHCO<sub>3</sub> aq. using gas-flow H-type cell. a) FE for CO<sub>2</sub> reduction products for Cu<sub>58</sub>-I NC-loaded catalysts at different applied potentials. b) FE for CO<sub>2</sub> reduction products for Cu<sub>58</sub>-II NC-loaded catalysts at different applied potentials. c) Comparisons of FE for Cu<sub>58</sub>-I NC and Cu<sub>58</sub> NC-loaded catalysts at −0.9 V versus RHE. Error bars representing the mean ± SD, *n* = 3. d) Current densities of different products obtained by Cu<sub>58</sub>-I NC-loaded catalyst. e) Current densities of different products obtained by Cu<sub>58</sub>-II NC-loaded catalyst. f) FE for Cu<sub>58</sub>-I NC-loaded catalysts under CO<sub>2</sub> or Ar flow at −0.9 V versus RHE.

formation (0.03 V vs RHE).<sup>[8d]</sup> These overvoltage differences likely contributed to the decrease in the formation efficiency of methanol ( $\text{FE}_{\text{CH}_3\text{OH}}$ ). In addition to the  $^1\text{H}$  NMR detection process, we further confirm the selective production of  $\text{CH}_3\text{OH}$ , through a GC-MS measurement. The electrolyte after  $\text{CO}_2\text{RR}$  exhibited only a peak at the same retention time (r.t. = 5.9 min) as the  $\text{CH}_3\text{OH}$  introduced as the standard sample, without other  $\text{CO}_2\text{RR}$  products. This peak showed a pattern with a  $m/z$  of 31, and the simulated fragment pattern based on electron ionization was consistent with that of  $\text{CH}_3\text{OH}$  (Figure S22, Supporting Information). By achieving the selectivity of  $\text{CO}_2\text{RR}$  products through precise control of defect-induced structural architecture, we demonstrated the exceptional catalytic activity of  $\text{Cu}_{58}\text{-I}$  NCs. Notably,  $\text{Cu}_{58}\text{-I}$  NCs are among a limited number of electrocatalysts capable of producing  $\text{CH}_3\text{OH}$  without concurrent  $\text{HCOOH}$  generation, underscoring its unique effectiveness.<sup>[19]</sup> However, at higher potentials, the decrease in selectivity may be linked to the loss of key intermediates, which limits the range of products formed. To further elucidate the catalytic properties of these NCs, we investigated them through theoretical calculations in the subsequent section. In our quest to

pinpoint the origin of carbon-based products, we conducted experiments by altering the feedstock source to argon (Ar) gas. Remarkably, under this condition, the detection of only  $\text{H}_2$  as a product suggests that the carbon-based products originate from the flowed  $\text{CO}_2$  feedstock rather than from impurities or contaminants in the system (Figure 5d). Additionally, we delved into assessing the stability of  $\text{Cu}_{58}\text{-I}$  NC through chronoamperometric measurements conducted at  $-0.9$  V. Intriguingly, the current density remained consistent over an extended period, with no discernible degradation observed for at least 6 h (Figure S23, Supporting Information). This highlights the robust stability of  $\text{Cu}_{58}\text{-I}$  NC under the applied electrochemical conditions, further underscoring its potential as a promising catalyst for sustained  $\text{CO}_2$  reduction reactions.

## 2.5. Density Functional Theory (DFT) Calculations and Mechanistic Insights

To correlate the selectivity difference between  $\text{Cu}_{58}$  and  $\text{Cu}_{58}\text{-I}$  NCs in electrochemical  $\text{CO}_2\text{RR}$  with their structural/active-site difference, we carried out DFT calculations based on the

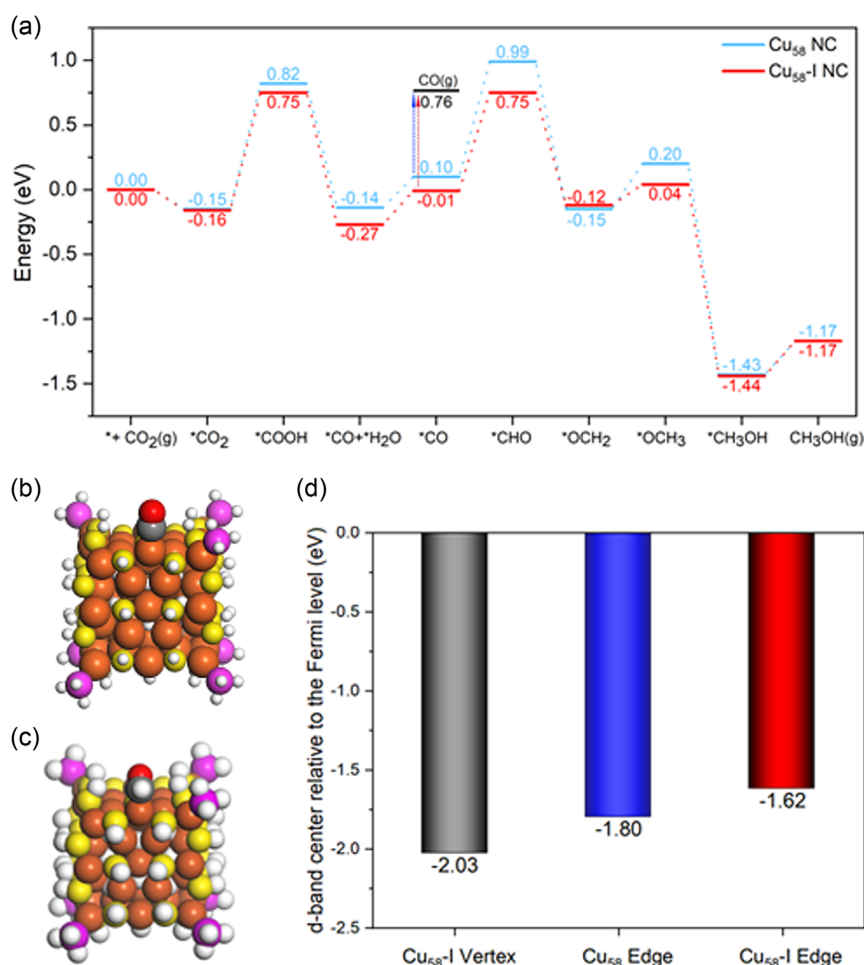


**Figure 6.** a) DFT-computed energy profile for  $\text{CO}_2\text{RR}$  on  $\text{Cu}_{58}\text{-I}$  NC (red) and  $\text{Cu}_{58}$  NC (blue); b) CO adsorbed on the  $\text{Cu}_{58}\text{-I}$  edge; c) CHO adsorbed on the  $\text{Cu}_{58}\text{-I}$  edge; d) d-band centers of the different Cu sites on the  $\text{Cu}_{58}\text{-I}$  and  $\text{Cu}_{58}$  NCs, computed from the local density of states. Color legend: Cu, brown; S, yellow; P, violet; H, white.

computational hydrogen electrode (see Supporting Information for details). We excluded Cu<sub>58</sub>-II nanoclusters from the study as HER is the main reaction pathway for this nanocluster. Our hypothesis is that at negative enough overpotentials, both catalysts can produce CO<sub>2</sub> to CO but only Cu<sub>58</sub>-I NC can further reduce CO to CH<sub>3</sub>OH. To test this hypothesis, we computed the detailed CO<sub>2</sub>RR pathway from CO<sub>2</sub> to CO and then to CH<sub>3</sub>OH on both Cu<sub>58</sub> and Cu<sub>58</sub>-I NCs. As shown in Figure 6a, we found that CO<sub>2</sub> is weakly adsorbed on both clusters. Then we used the computational hydrogen electrode method and sequentially added H to CO<sub>2</sub> and computed the intermediate adsorption energies. We found that the formation of \*COOH is more favorable than \*HCOO (Figure S24, Supporting Information) and less uphill on Cu<sub>58</sub>-I than Cu<sub>58</sub>. The next step is CO formation from \*COOH, which significantly favors Cu<sub>58</sub>-I over Cu<sub>58</sub>. After H<sub>2</sub>O desorption, \*CO is converted to \*CHO, which is the potential-limiting step leading to CH<sub>3</sub>OH formation. On the Cu<sub>58</sub> NC, CO desorption is easier than \*CHO formation, while on the Cu<sub>58</sub>-I NC, \*CHO is competitive against CO desorption. CO and CHO adsorb stronger on the Cu<sub>58</sub>-I NC than on the Cu<sub>58</sub> NC. We think that this is a key reason why Cu<sub>58</sub>-I can catalyze CO<sub>2</sub>RR to CH<sub>3</sub>OH, while Cu<sub>58</sub> cannot. More interestingly, we found that CO and CHO actually adsorb on the edge Cu site next to the defect Cu site (Figure 6b,c), but on the defect vertex Cu site. In other words, the inward movement of the Cu(I) atom and the missing phosphine ligand at the vertex site rendered the nearby edge Cu sites more reactive. To further understand the intricate connection between the geometric and electronic factors here, we analyzed the local density of states at the different Cu sites (Figure S25, Supporting Information) and found that the d-band center of the edge site on Cu<sub>58</sub>-I shifted up in comparison with the edge site on Cu<sub>58</sub> and the defect vertex site on Cu<sub>58</sub>-I (Figure 6d), indicating a higher reactivity.

## 2.6. Sustainability of the NC

The stability of the Cu<sub>58</sub>-I NC was further confirmed by comparing the size of individual NCs before and after the electrocatalytic reaction within a CB matrix through TEM measurements, which provided insights into its structural integrity (Figure S26, Supporting Information). Furthermore, X-ray photoelectron spectroscopy (XPS) investigations confirmed the stability of the metal atom valency of this NC both before and after the electrocatalytic reaction (Figure S27, Supporting Information). Consistently, the deconvolution of the binding energies of Cu 2p<sub>3/2</sub> at 932.8 eV and Cu 2p<sub>1/2</sub> at 952.6 eV, along with a subtle satellite signal, persisted across the spectrum which indicates the presence of Cu(I) species.

## 3. Conclusion

In summary, herein we reported a novel synthesis method for a surface ligand vacancy-induced Cu NCs, distinguished by their unique arrangement of metal atoms, deviating from the conventional regular configuration. The structural distortions significantly influence their catalytic behavior, particularly in electrochemical CO<sub>2</sub>RR. Through our electrochemical analyses,

we have discovered an exceptional selectivity for CH<sub>3</sub>OH production (FE<sub>CH<sub>3</sub>OH</sub> is ≈54% at −0.7 V vs RHE), marking the defect-induced Cu<sub>58</sub>-I NC as the first to demonstrate direct electrochemical conversion of such product using NCs. In contrast, the regular Cu<sub>58</sub> NCs primarily produce CO, while the additional defects in the structural architecture promote HER pathways. DFT calculations of the CO<sub>2</sub>RR pathways attributed the selectivity toward CH<sub>3</sub>OH to enhanced binding of CO and CHO intermediates at the edge Cu site next to the vertex Cu site with a ligand vacancy; electronic structure analysis showed that the d-states of the edge Cu site shifted up due to the geometric distortion induced by the defect and the missing phosphine ligand, rendering the edge Cu site more active. Thus, this comprehensive approach not only elucidates the catalytic mechanism but also underscores the potential of tailored structural designs for enhancing electrochemical CO<sub>2</sub> reduction efficiency.

## Supporting Information

Supporting Information is available from the Wiley Online Library or from the author.

## Acknowledgements

Y.N. acknowledges the financial support of the JSPS KAKENHI (grant no. 23H00289 and 22K19012), Scientific Research on Innovative Areas "Aquatic Functional Materials" (grant no. 22H04562), the Yazaki Memorial Foundation for Science and Technology, Advanced Technology Institute Research Grants, Takahashi Industrial and Economic Research Foundation, and the Kumagai Foundation for Science and Technology and the Ogasawara Foundation for the Promotion of Science and Engineering. DFT computation (H.S. and D.J.) was supported by the U.S. Department of Energy, Office of Science, Office of Basic Energy Sciences, Chemical Sciences, Geosciences, and Biosciences Division, Catalysis Science Program.

## Conflict of Interest

The authors declare no conflict of interest.

## Author Contributions

**Sourav Biswas:** Conceptualization (equal); Investigation (lead); Writing—original draft (lead). **Tomoya Tanaka:** Investigation (equal). **Haohong Song:** Investigation (supporting). **Masaki Ogami:** Investigation (supporting). **Yamato Shingyouchi:** Investigation (supporting). **Sakiat Hossian:** Investigation (supporting). **Maho Kamiyama:** Investigation (supporting). **Taiga Kosaka:** Investigation (supporting). **Riki Nakatani:** Investigation (supporting). **Yoshiki Niihori:** Investigation (supporting). **Saikat Das:** Investigation (supporting). **Tokuhiisa Kawawaki:** Conceptualization (lead); Writing—original draft (lead). **De-en Jiang:** Conceptualization (supporting); Writing—review and editing (equal). **Yuichi Negishi:** Conceptualization (lead); Funding acquisition (lead); Project administration (lead); Resources (lead); Supervision (lead); Writing—review and editing (lead).

## Data Availability Statement

The data that support the findings of this study are available from the corresponding author upon reasonable request.



## Keywords

catalysis, copper, crystal structure, density functional theory, nanoclusters, thiolate

Received: September 10, 2024

Revised: November 14, 2024

Published online:

- [1] S. J. Davis, K. Caldeira, H. D. Matthews, *Science* **2010**, 329, 1330.
- [2] G. A. Olah, G. S. Prakash, A. Goepfert, *J. Am. Chem. Soc.* **2011**, 133, 12881.
- [3] a) F. A. Rahman, M. M. A. Aziz, R. Saidur, W. A. W. A. Bakar, M. Hainin, R. Putrajaya, N. A. Hassan, *Renewable Sustainable Energy Rev.* **2017**, 71, 112; b) A. Goepfert, M. Czaun, G. S. Prakash, G. A. Olah, *Energy Environ. Sci.* **2012**, 5, 7833; c) A. Saravanan, D.-V. N. Vo, S. Jeevanantham, V. Bhuvaneswari, V. A. Narayanan, P. Yaashikaa, S. Swetha, B. Reshma, *Chem. Eng. Sci.* **2021**, 236, 116515.
- [4] E. E. Benson, C. P. Kubiak, A. J. Sathrum, J. M. Smieja, *Chem. Soc. Rev.* **2009**, 38, 89.
- [5] a) B. Kumar, J. P. Brian, V. Atla, S. Kumari, K. A. Bertram, R. T. White, J. M. Spurgeon, *Catal. Today* **2016**, 270, 19; b) S. Yu, S. Louisia, P. Yang, *JACS Au* **2022**, 2, 562.
- [6] F. Franco, C. Rettenmaier, H. S. Jeon, B. R. Cuenya, *Chem. Soc. Rev.* **2020**, 49, 6884.
- [7] P. Saha, S. Amanullah, A. Dey, *Acc. Chem. Res.* **2022**, 55, 134.
- [8] a) H. Liu, Y. Zhu, J. Ma, Z. Zhang, W. Hu, *Adv. Funct. Mater.* **2020**, 30, 1910534; b) K. Kwak, D. Lee, *Acc. Chem. Res.* **2018**, 52, 12; c) D. Yang, J. Wang, Q. Wang, Z. Yuan, Y. Dai, C. Zhou, X. Wan, Q. Zhang, Y. Yang, *ACS Nano* **2022**, 16, 15681; d) T. Kawawaki, T. Okada, D. Hirayama, Y. Negishi, *Green Chem.* **2024**, 26, 122; e) J. Huang, N. Hörmann, E. Oveis, A. Loidice, G. L. De Gregorio, O. Andreussi, N. Marzari, R. Buonsanti, *Nat. Commun.* **2018**, 9, 3117; f) Z. Liu, J. Chen, B. Li, D.-E. Jiang, L. Wang, Q. Yao, J. Xie, *J. Am. Chem. Soc.* **2024**, 146, 11773.
- [9] a) Y. Sun, X. Liu, K. Xiao, Y. Zhu, M. Chen, *ACS Catal.* **2021**, 11, 11551; b) H. Seong, V. Efremov, G. Park, H. Kim, J. S. Yoo, D. Lee, *Angew. Chem. Int. Ed.* **2021**, 60, 14563; c) S. Zhao, R. Jin, R. Jin, *ACS Energy Lett.* **2018**, 3, 452; d) J. Wang, F. Xu, Z. Y. Wang, S. Q. Zang, T. C. Mak, *Angew. Chem. Int. Ed.* **2022**, 61, e202207492; e) H. Seong, M. Choi, S. Park, H.-W. Kim, J. Kim, W. Kim, J. S. Yoo, D. Lee, *ACS Energy Lett.* **2022**, 7, 4177; f) Y. Qiu, Z. Xie, S. Gao, H. Cao, S. Zhang, Q. Liu, X. Liu, J. Luo, *ChemElectroChem* **2022**, 9, e202200987; g) T. Kawawaki, Y. Kataoka, M. Hirata, Y. Akinaga, R. Takahata, K. Wakamatsu, Y. Fujiki, M. Kataoka, S. Kikkawa, A. S. Alotabi, S. Hossain, D. J. Osborn, T. Teranishi, G. G. Andersson, G. F. Metha, S. Yamazoe, Y. Negishi, *Angew. Chem. Int. Ed.* **2021**, 60, 21340; h) B. Kumar, T. Kawawaki, N. Shimizu, Y. Imai, D. Suzuki, S. Hossain, L. V. Nair, Y. Negishi, *Nanoscale* **2020**, 12, 9969; i) L. Sun, V. Reddu, X. Wang, *Chem. Soc. Rev.* **2022**, 51, 8923; j) G. Deng, H. Yun, M. S. Bootharaju, F. Sun, K. Lee, X. Liu, S. Yoo, Q. Tang, Y. J. Hwang, T. Hyeon, *J. Am. Chem. Soc.* **2023**, 145, 27407; k) J. Hu, M. Zhou, K. Li, A. Yao, Y. Wang, Q. Zhu, Y. Zhou, L. Huang, Y. Pei, Y. Du, S. Jin, M. Zhu, *Small* **2023**, 19, 2301357; l) L. Li, Y. Lv, H. Sheng, Y. Du, H. Li, Y. Yun, Z. Zhang, H. Yu, M. Zhu, *Nat. Commun.* **2023**, 14, 6989; m) S. Su, Y. Zhou, L. Xiong, S. Jin, Y. Du, M. Zhu, *Angew. Chem. Int. Ed.* **2024**, 63, e202404629.
- [10] T. J. Dekka, A. I. Osman, D. C. Baruah, D. W. Rooney, *Environ. Chem. Lett.* **2022**, 20, 3525.
- [11] a) S. Navarro-Jaén, M. Virginie, J. Bonin, M. Robert, R. Wojcieszak, A. Y. Khodakov, *Nat. Rev. Chem.* **2021**, 5, 564; b) I. Hussain, H. Alasiri, W. U. Khan, K. Alhooshani, *Coord. Chem. Rev.* **2023**, 482, 215081; c) S. Kong, X. Lv, X. Wang, Z. Liu, Z. Li, B. Jia, D. Sun, C. Yang, L. Liu, A. Guan, *Nat. Catal.* **2023**, 6, 6.
- [12] a) S. Biswas, S. Das, Y. Negishi, *Nanoscale Horiz.* **2023**, 8, 1509; b) Y. Liu, J. Yu, Y. Lun, Y. Wang, Y. Wang, S. Song, *Adv. Funct. Mater.* **2023**, 33, 2304184; c) Y. Ma, M. Sun, H. Xu, Q. Zhang, J. Lv, W. Guo, F. Hao, W. Cui, Y. Wang, J. Yin, H. Wen, P. Lu, G. Wang, J. Zhou, J. Yu, C. Ye, L. Gan, D. Zhang, S. Chu, L. Gu, M. Shao, B. Huang, Z. Fan, *Adv. Mater.* **2024**, 36, 2402979; d) J. Wang, M. Sun, H. Xu, F. Hao, Q. Wa, J. Su, J. Zhou, Y. Wang, J. Yu, P. Zhang, R. Ye, S. Chu, B. Huang, M. Shao, Z. Fan, *ACS Nano* **2024**, 18, 7192; e) L. Guo, J. Zhou, F. Liu, X. Meng, Y. Ma, F. Hao, Y. Xiong, Z. Fan, *ACS Nano* **2024**, 18, 9823; f) Y. Ma, J. Yu, M. Sun, B. Chen, X. Zhou, C. Ye, Z. Guan, W. Guo, G. Wang, S. Lu, D. Xia, Y. Wang, Z. He, L. Zheng, Q. Yun, L. Wang, J. Zhou, P. Lu, J. Yin, Y. Zhao, Z. Luo, L. Zhai, L. Liao, Z. Zhu, R. Ye, Y. Chen, Y. Lu, S. Xi, B. Huang, C. Lee, Z. Fan, *Adv. Mater.* **2022**, 34, 2110607; g) Y. Ma, J. Wang, J. Yu, J. Zhou, X. Zhou, H. Li, Z. He, H. Long, Y. Wang, P. Lu, J. Yin, H. Sun, Z. Zhang, Z. Fan, *Matter* **2021**, 4, 888.
- [13] a) Q. Tang, Y. Lee, D.-Y. Li, W. Choi, C. W. Liu, D. Lee, D.-E. Jiang, *J. Am. Chem. Soc.* **2017**, 139, 9728; b) L.-J. Liu, Z. Y. Wang, Z.-Y. Wang, R. Wang, S.-Q. Zang, T. C. W. Mak, *Angew. Chem. Int. Ed.* **2022**, 61, e202205626; c) D. Chen, L. H. Zhang, J. Du, H. Wang, J. Guo, J. Zhan, F. Li, F. Yu, *Angew. Chem. Int. Ed.* **2021**, 60, 24022; d) Q.-J. Wu, D.-H. Si, P.-P. Sun, Y.-L. Dong, S. Zheng, Q. Chen, S.-H. Ye, D. Sun, R. Cao, Y.-B. Huang, *Angew. Chem. Int. Ed.* **2023**, 62, e202306822; e) F. Li, Q. Tang, *J. Catal.* **2020**, 387, 95; f) Y. F. Bu, M. Zhao, G. X. Zhang, X. Zhang, W. Gao, Q. Jiang, *ChemElectroChem* **2019**, 6, 1831; g) C. Liu, X.-D. Zhang, J.-M. Huang, M.-X. Guan, M. Xu, Z.-Y. Gu, *ACS Catal.* **2022**, 12, 15230; h) L. Zhang, X.-X. Li, Z.-L. Lang, Y. Liu, J. Liu, L. Yuan, W.-Y. Lu, Y.-S. Xia, L.-Z. Dong, D.-Q. Yuan, *J. Am. Chem. Soc.* **2021**, 143, 3808.
- [14] Y. Yang, S. Louisia, S. Yu, J. Jin, I. Roh, C. Chen, M. V. Fonseca Guzman, J. Feijóo, P.-C. Chen, H. Wang, *Nature* **2023**, 614, 262.
- [15] a) M. Ding, L. Tang, X. Ma, C. Song, S. Wang, *Commun. Chem.* **2022**, 5, 172; b) S. Biswas, A. Pal, M. K. Jena, S. Hossain, J. Sakai, S. Das, B. Sahoo, B. Pathak, Y. Negishi, *J. Am. Chem. Soc.* **2024**, 146, 20937; c) A. K. Das, S. Biswas, A. Pal, S. S. Manna, A. Sardar, P. K. Mondal, B. Sahoo, B. Pathak, S. Mandal, *Nanoscale* **2024**, 16, 3583.
- [16] a) C. Dong, R. W. Huang, A. Sagadevan, P. Yuan, L. Gutiérrez-Arzaluz, A. Ghosh, S. Nematullov, B. Alamer, O. F. Mohammed, I. Hussain, M. Rueping, O. M. Bakr, *Angew. Chem. Int. Ed.* **2023**, 62, e202307140; b) S. Nematullov, A. Sagadevan, B. Alamer, A. Shkurenko, R. Huang, J. Yin, C. Dong, P. Yuan, K. E. Yarov, A. A. Karluk, W. J. Mir, B. E. Hasanov, M. Nejib Hedhili, N. M. Halappa, M. Eddaoudi, O. F. Mohammed, M. Rueping, O. M. Bakr, *Angew. Chem. Int. Ed.* **2023**, 62, e202303572.
- [17] S. Biswas, S. Hossain, T. Kosaka, J. Sakai, D. Arima, Y. Niihori, M. Mitsui, D. Jiang, S. Das, S. Wang, Y. Negishi, *Chem. Commun.* **2023**, 59, 9336.
- [18] a) S. Nematullov, A. Sagadevan, B. Alamer, A. Shkurenko, R. Huang, J. Yin, C. Dong, P. Yuan, K. E. Yarov, A. A. Karluk, W. J. Mir, B. E. Hasanov, M. N. Hedhili, N. M. Halappa, M. Eddaoudi, O. F. Mohammed, M. Rueping, O. M. Bakr, *Angew. Chem. Int. Ed.* **2023**, 62, e202303572; b) J. M. Pettibone, J. W. Hudgens, *ACS Nano* **2011**, 5, 2989.
- [19] a) P. Li, J. Bi, J. Liu, Q. Zhu, C. Chen, X. Sun, J. Zhang, B. Han, *Nat. Commun.* **2022**, 13, 1965; b) D. Yang, Q. Zhu, C. Chen, H. Liu, Z. Liu, Z. Zhao, X. Zhang, S. Liu, B. Han, *Nat. Commun.* **2019**, 10, 677.